Wave-matching-simulations of integrated optical coupler structures

M. Lohmeyer, N. Bahlmann, O. Zhuromskyy, P. Hertel*
Department of Physics, University of Osnabrück,
Barbarastraße 7, D-49069 Osnabrück, Germany

Abstract: Accurate calculation of guided modes is one of the principal tasks of numerically simulating integrated optical devices. Our recently proposed 'wave-matching-method' for dielectric waveguides with rectangular and piecewise constant refractive index profiles is based on expansions of the electromagnetic field into functions with harmonic and exponential dependence on the transverse coordinates. Local expansions for regions with constant permittivity are joined by minimizing a least squares expression for the remaining misfit at the discontinuity lines. We apply the wave-matching analysis to a number of more complex structures: a conventional, deeply etched two-waveguide coupler, an ARROW-waveguide, a three dimensional four-waveguide coupler and a three-waveguide coupler with multimode central rib.

Keywords: integrated optics, dielectric waveguides, coupler structures, guided modes, numerical modeling
PACS codes: 42.82 42.82.E 42.82.Et

1 Introduction

Frequently, interfering guided modes constitute the basis for integrated optical coupler devices. For devices comprising extended longitudinal homogeneous sections, any method by which the field of the entire structure is calculated directly suffers from less approximations than indirect methods, such as beam propagation [1, 2] or coupled mode theory [3]. Recent overviews over the variety of proposed mode solvers can be found in e.g. Refs. [4, 5].

Many coupler structures are fabricated by etching processes. The resulting permittivity profiles are piecewise constant, with the dielectric boundaries parallel to the transverse coordinate axes. While usually such waveguides are chosen as benchmark examples [5], most approaches (methods based on finite differences or finite elements, or the method of lines [6]) do not exploit the feature of piecewise constant refractive indices (an exception is the modal transverse resonance technique [7]). In contrast, the recently proposed wave matching method [8, 9] (WMM) is based directly on a decomposition as shown in Figure 1.

It is motivated by the common strategy for solving the mode problem for multilayer slab waveguides: On each region with constant refractive index a set of plausible solutions to the basic wave equation is selected. Then the boundary conditions for dielectric interfaces combine fields on neigboring regions to a system of linear equations. Its nonvanishing solutions yield propagation constants and mode profiles. The approach discussed in the following section may be regarded as an attempt for an extension to two transverse dimensions. For a fixed ansatz of trial fields the algorithm tries to find the best solution in terms of a least squares expression for the remaining mismatch on the dielectric boundaries.

For a number of simple raised strip and rib structures including standard benchmark problems, the method has been shown to be adequate, both for semivectorial [8] and fully vectorial simulations [9]. However, real integrated optical devices will include more complex cross sections, and therefore, in Section 3 of this paper, we investigate applying the WMM to several more involved coupler structures. Due to the need of computing higher order as well as fundamental modes, and due to a usually large relevant part of the waveguide cross section plane, these tasks bear additional difficulties for most mode solvers.

* *Fachbereich Physik, Universität Osnabrück* *Barbarastraße 7, D 49069 Osnabrück*
Tel.: +541/969-2641 *Fax: +541/969-2670* *e-mail: manfred.lohmeyer@physik.uni-osnabrueck.de*

2 Wave-matching-method

Figure 1 shows an example for the cross section of a lossless longitudinal homogeneous structure with piecewise constant isotropic real permittivity $\epsilon = n^2$.

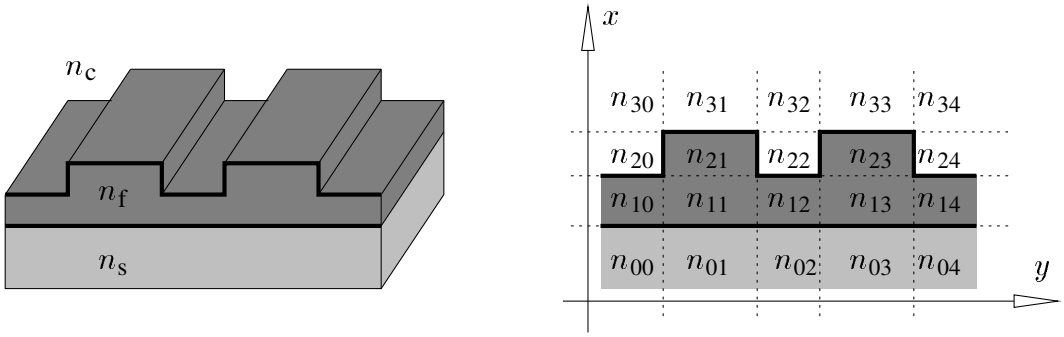

Figure 1: Typical coupler geometry. The cross section may be divided into rectangular regions with constant refractive indices n_{lm}. The boundaries are parallel to the transverse coordinate axes x and y.

The electric field $\boldsymbol{\mathcal{E}}$ and magnetic field $\boldsymbol{\mathcal{H}}$ of guided, in general hybrid modes have the form

$$\boldsymbol{\mathcal{E}}(x,y,z,t) = \begin{pmatrix} E_x \\ E_y \\ \mathrm{i}E_z \end{pmatrix}(x,y)\ \mathrm{e}^{\mathrm{i}(\omega t - \beta z)}, \quad \boldsymbol{\mathcal{H}}(x,y,z,t) = \begin{pmatrix} H_x \\ H_y \\ \mathrm{i}H_z \end{pmatrix}(x,y)\ \mathrm{e}^{\mathrm{i}(\omega t - \beta z)}. \tag{1}$$

Fields propagate with wavenumber β in z direction, at an angular frequency $\omega = kc = 2\pi c/\lambda$ given by the speed of light c and the vacuum wavelength λ. Without loss of generality, the square integrable components E_x to H_z of the mode profiles may be chosen to be real.

With the mode ansatz Eq. (1) inserted into Maxwell's equations, the longitudinal components can be expressed in terms of the transverse components by the divergence relations. Additionally, the curl equations allow to eliminate two further components. Standard formulations for the fully vectorial mode problem employ either the two transverse electric, the two tranverse magnetic, or the two longitudinal components as basic fields. Only these two fields have to be calculated directly.

If the analysis is restricted to the semivectorial approximation, usually for TE polarized modes, the minor component E_x is assumed to vanish, while TM polarized modes have a vanishing H_x component. In this approximation, merely one basic field remains.

Inside the regions (index r) with constant permittivity ϵ^r, all mode components ϕ satisfy the Helmholtz wave equation

$$\partial_x^2\phi + \partial_y^2\phi = (\beta^2 - k^2\epsilon^r)\phi. \tag{2}$$

Thus we can choose an ansatz of factorizing functions, superposed with coefficients a^r_{lj}, separately for each basic component ϕ_l and on each rectangular region:

$$\phi_l(x,y) = \sum_j a^r_{lj}\, c^r_{lj}\, F^r_{lj}(p^r_{lj}(x - x^r_{0,lj}))\, G^r_{lj}(q^r_{lj}(y - y^r_{0,lj})). \tag{3}$$

In the following, indices l, j, r are omitted for brevity. F and G are one of the functions sin, cos, or exp. c is a normalization constant and x_0 and y_0 are introduced as local coordinate offsets to handle the exponential functions numerically. Then valid pairs (p, q) of the transverse wave vector components p and q lie on curves defined by the equation

$$\pm p^2 \pm q^2 = \beta^2 - k^2\epsilon, \tag{4}$$

with the signs depending on the choice of F and G. While all points (p, q) satisfying Eq. (4) yield valid trial functions, numerically only a suitable discrete set can be implemented. Therefore, a number of discrete points

(p_j, q_j) from the curves (4) must be selected, each one defining a contribution j to the sum (3). This is done separately for every basic component, for all rectangular parts of the cross section, for every pair of choices of F and G, and with two constraints: the selected points should cover the entire relevant domain on the curve (4), i.e. the space spanned by the corresponding trial functions must be sufficiently large, while at the same time these functions must be numerically linearly independent. In Ref. [8] a somehow universal procedure for this nonequidistant spectral discretization is described in detail.

On the first and last rectangle of each line and column in the cross section decomposition Figure 1 this procedure is applied considering only outwards exponetially decaying trial functions. This implements the constraint of a square integrable mode field without any further boundary conditions. No spatial computational window is required.

Once the systems of trial functions are established on the separate rectangular regions, these regions are to be joined by employing the continuity conditions for electromagnetric fields on dielectric boundaries, as summarized in Table 1.

		Quantities continuous on	
	Basic fields	horizontal boundaries	vertical boundaries
TE	E_y	E_y, $\partial_x E_y$	ϵE_y, $\partial_y E_y$
TM	H_y	H_y, $\epsilon^{-1}\partial_x H_y$	H_y, $\partial_y H_y$
VEC	E_x, E_y, or H_x, H_y, or E_z, H_z	ϵE_x, E_y, E_z, H_x, H_y, H_z	E_x, ϵE_y, E_z, H_x, H_y, H_z

Table 1: Basic fields and boundary conditions for calculating semivectorial TE and TM polarized modes and for fully vectorial mode analysis.

Indicating by C_h all horizontal and by C_v all vertical boundaries on the cross section plane, we establish a least squares expression D for the misfit of the fields on the boundary lines. It is to be considered a function of the trial value β for the propagation constant, and of the vector $\boldsymbol{a}$ of coefficients from Eq. (3). For semivectorial TE calculations, this reads

$$\begin{aligned} D_\beta(\boldsymbol{a}) &= \int_{C_h} \left\{ \left(E_y^+ - E_y^-\right)^2 + \left(\frac{1}{k}\partial_x E_y^+ - \frac{1}{k}\partial_x E_y^-\right)^2 \right\} \mathrm{d}y \\ &+ \int_{C_v} \left\{ \left(\frac{2\epsilon^+}{\epsilon^+ + \epsilon^-} E_y^+ - \frac{2\epsilon^-}{\epsilon^+ + \epsilon^-} E_y^-\right)^2 + \left(\frac{1}{k}\partial_y E_y^+ - \frac{1}{k}\partial_y E_y^-\right)^2 \right\} \mathrm{d}x\,. \end{aligned} \tag{5}$$

The analogous expression for TM polarization is

$$\begin{aligned} D_\beta(\boldsymbol{a}) &= \int_{C_h} \left\{ \left(H_y^+ - H_y^-\right)^2 + \left(\frac{1}{k\epsilon^+}\partial_x H_y^+ - \frac{1}{k\epsilon^-}\partial_x H_y^-\right)^2 \right\} \mathrm{d}y \\ &+ \int_{C_v} \left\{ \left(H_y^+ - H_y^-\right)^2 + \left(\frac{\epsilon^- + \epsilon^+}{2k\epsilon^-\epsilon^+}\partial_y H_y^+ - \frac{\epsilon^- + \epsilon^+}{2k\epsilon^-\epsilon^+}\partial_y H_y^-\right)^2 \right\} \mathrm{d}x\,. \end{aligned} \tag{6}$$

For fully vectorial calculations, squared deviations in all six components are summed:

$$\begin{aligned} D_\beta(\boldsymbol{a}) &= \sqrt{\epsilon_0} \int_{C_h} \left\{ (\epsilon^+ E_x^+ - \epsilon^- E_x^-)^2 + (E_y^+ - E_y^-)^2 + (E_z^+ - E_z^-)^2 \right\} \mathrm{d}y \\ &+ \sqrt{\mu_0} \int_{C_h} \left\{ (H_x^+ - H_x^-)^2 + (H_y^+ - H_y^-)^2 + (H_z^+ - H_z^-)^2 \right\} \mathrm{d}y \\ &+ \sqrt{\epsilon_0} \int_{C_v} \left\{ (E_x^+ - E_x^-)^2 + (\epsilon^+ E_y^+ - \epsilon^- E_y^-)^2 + (E_z^+ - E_z^-)^2 \right\} \mathrm{d}x \\ &+ \sqrt{\mu_0} \int_{C_v} \left\{ (H_x^+ - H_x^-)^2 + (H_y^+ - H_y^-)^2 + (H_z^+ - H_z^-)^2 \right\} \mathrm{d}x\,. \end{aligned} \tag{7}$$

Here superscripts $+$ and $-$ indicate fields assigned to adjacent rectangles on opposite sides of the boundary, where the functions are evaluated exactly on the boundary line. In Eq. (7), all components are meant to be

expressed by the two basic fields. The roots of the vacuum permittivity ϵ_0 and permeability μ_0 in Eq. (7), and the inverse wavenumbers k and the permittivity averages in Eq. (5), Eq. (6) have been introduced to adjust the dimensions of the fields and their derivatives and of the electric and magnetic components, and in order to equilibrate contributions from horizontal and vertical boundaries. While these factors are chosen somewhat arbitrarily (cf. the corresponding remarks in Refs. [8, 9]), vanishing $D_\beta(\boldsymbol{a})$ guarantees that $\boldsymbol{a}$ and β describe a guided mode exactly.

With a restricted set of ansatz functions, one can not expect an exact solution. To compare them with respect to the mismatch on the boundaries, the trial solutions have to be normalized. For this purpose, we adopted the common expressions

$$N_\beta(\boldsymbol{a}) = \iint E_y^2 \,\mathrm{d}x\,\mathrm{d}y \tag{8}$$

for semivectorial TE and

$$N_\beta(\boldsymbol{a}) = \iint \frac{1}{\epsilon} H_y^2 \,\mathrm{d}x\,\mathrm{d}y \tag{9}$$

for semivectorial TM calculations. Fully vectorial fields were normalized with respect to one of the expressions

$$N_\beta(\boldsymbol{a}) = \iint \left\{E_x^2 + E_y^2 + E_z^2\right\} \,\mathrm{d}x\,\mathrm{d}y \quad \text{or} \quad N_\beta(\boldsymbol{a}) = \iint \left\{H_x^2 + H_y^2 + H_z^2\right\} \,\mathrm{d}x\,\mathrm{d}y\,. \tag{10}$$

The integrals are meant to be evaluated piecewise over the rectangles of the cross section decomposition. Remarks with respect to the arbitrary chosen error expressions apply to the normalization as well. Note that for the fully vectorial case the longitudinal component of the Poynting vector does not yield a positive definite form suitable for normalization.

With the expressions for the least squares error and for the normalization, the WMM implements the following procedure. For a given trial value of the propagation constant β, one calculates that vector of coefficients $\boldsymbol{a}$, normalized as $N_\beta(\boldsymbol{a}) = 1$, which yields the minimum error $\mu_\beta = D_\beta(\boldsymbol{a})$, i.e. meets the boundary conditions best. If the trial value β is close to a valid propagation constant, one can expect the remaining misfit to become small. Therefore, this remaining misfit μ_β is minimized with respect to the trial value β. The minima identify the approximations to the propagation constants computed by the WMM. The corresponding optimal coefficient vector $\boldsymbol{a}$ represents the modal field.

If the ansatz Eq. (3) is inserted into Eqs. (5)–(7) and Eqs. (8)–(10), the expressions for the boundary mismatch and norm both reduce to quadratic forms

$$D_\beta(\boldsymbol{a}) = \boldsymbol{a}^\mathsf{T} \mathsf{D}_\beta \boldsymbol{a}, \quad N_\beta(\boldsymbol{a}) = \boldsymbol{a}^\mathsf{T} \mathsf{N}_\beta \boldsymbol{a}, \tag{11}$$

where D_β and N_β are positive real matrices. Consequently, solving the generalized eigenvalue equation

$$\mathsf{D}_\beta \boldsymbol{a} = \mu_\beta \mathsf{N}_\beta \boldsymbol{a} \tag{12}$$

for the smallest eigenvalue gives the lowest achievable error for a trial value β. Details of the numerical procedure owing to the special structure of the matrices involved have been discussed in Ref. [8]. Note that μ_β must be minimized with respect to β, i.e. multiple evaluations of Eq. (11) are required.

For the fully vectorial calculation of a simple raised strip waveguide, Figure 2 illustrates the behaviour of this error function μ_β. It consists of parabolic sections, each with a valid propagation constant at the minimum. The waveguide supports four guided modes with a definite symmetry with respect to $y \to -y$. A field ansatz [9] with H_x, E_y, H_z even and E_x, H_y, E_z odd yields the hybrid modes TE_0 and TM_1, classified by the dominant components and their vertical nodal lines. An ansatz of opposite symmetry gives the lowest order TM and first order TE mode. If no symmetry is prescribed, the least squares error function shows minima corresponding to all four modes.

The propagation constants given in the caption of Figure 2 are stable with respect to the choice of the normalization expression Eq. (10), with respect to the choice of the two basic fields for the vectorial mode problem,

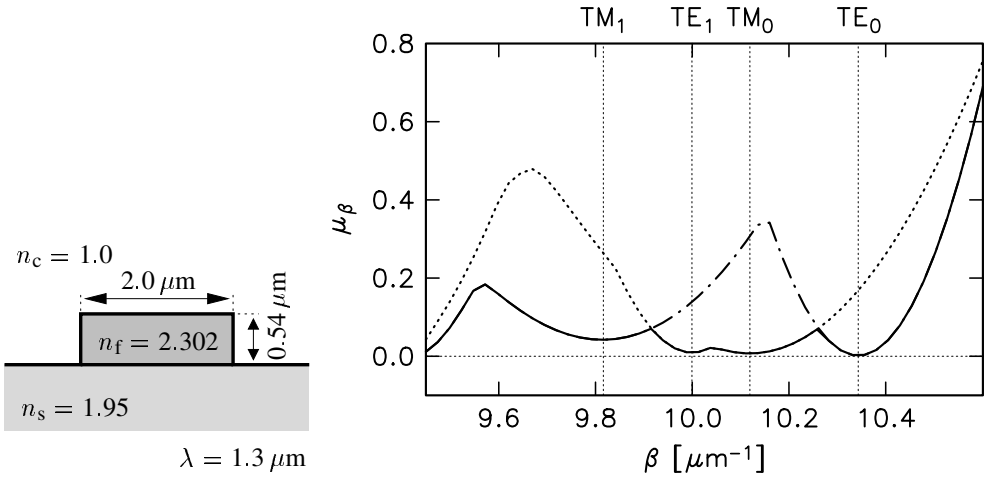

Figure 2: For a raised strip waveguide as sketched in the left inset: remaining least squares error μ_β versus the trial value β for the propagation constant. The continuous line corresponds to fields without prescribed symmetry, the dash-dotted and dotted lines (partially shadowed) to fields with even and odd symmetry (see the text). The propagation constants $\beta/\,\mu\text{m}^{-1}$ indicated by the minima locations are 10.3432 *(TE$_0$),* 10.1192 *(TM$_0$),* 9.9994 *(TE$_1$), and* 9.8162 *(TM$_1$).*

and with respect to refinement of the spectral discretization [9]. The calculations with prescribed symmetry involved about 650 unknowns, where identifying the fundamental vectorial mode takes about 10 min and 6 MB of memory on a 99 MHz HP-735 computer. Switching to the semivectorial approximation reduces this to about 1 min and half the number of unknowns, and yields a value of $10.3442\,\mu\text{m}^{-1}$ for the propagation constant. For a more detailed assessment involving standard benchmark problems see Refs. [8, 9].

Frequently, splitting the mode set into two subsets of opposite symmetry allows to separate modes with closely spaced propagation constants. Despite their shallow appearance, evaluation of the minima in Figure 2 to sufficient precision has never been a problem. However, at some instances even modes with equal symmetry happen to propagate at almost the same wavenumber. One such case is illustrated in Figure 2, where the hybrid first order TE and zeroth order TM modes are almost degenerate (this occurs for slightly varied parameters and leads to polarization conversion [10]). A possible ansatz to handle these structures is to use the freedom in the choice of the normalization expression to identify the parabolic sections in the error function μ_β corresponding to the degenerate modes (cf. the remarks at the end of Section 3).

3 Numerical results

At present, the WMM has been implemented to handle cross section decompositions as in Figure 1 with an arbitrary number of horizontal and vertical boundary lines. In practice, the computational effort scales strongly with the number of rectangles, if the spectral discretization is not decreased. Therefore, discretizing a continuously varying refractive index profile or a profile with not rectangular boundaries is not an option. WMM treatment of such structures would require a major reformulation.

At the same time, a number of interesting structures comprise *few* rectangles and boundary lines only, with quite different mode profiles and working principles. Four examples will be presented in the following sections.

3.1 Two waveguide coupler

The first one is a conventional two waveguide coupler as sketched in Figure 3 with parameters taken from Ref. [11]. Between the two ribs, the film is assumed to be etched less than beside, resulting in strong coupling.

The slab waveguide corresponding to the central region (thickness $0.7\,\mu$m, refractive indices 1.458, 1.644, 1.0, wavelength $0.633\,\mu$m) already guides two planar TE and two TM modes, and therefore the rib structure supports more than two modes for each polarization. While in general all these modes contribute to the guided field, only the two fundamental ones will be excited, if power is inserted by one single moded port waveguide.

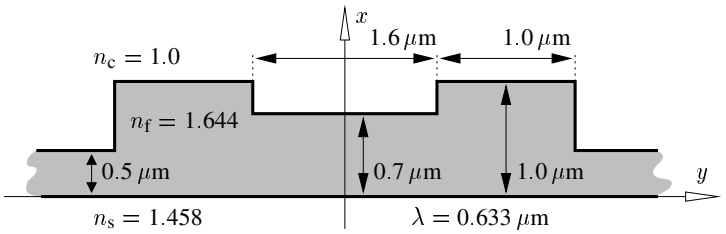

Figure 3: Parameters for the two rib waveguide coupler.

Figure 4 illustrates these two modes for TE polarization, each computed with a semivectorial field ansatz of proper symmetry.

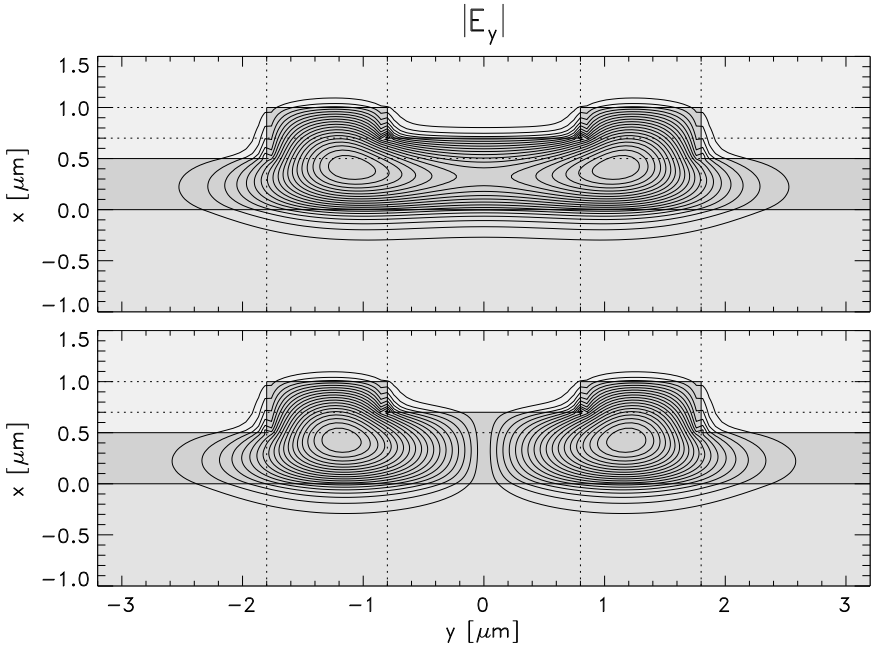

Figure 4: Field profiles for the coupler of Figure 3. The contours correspond to the dominant component $|E_y|$ of the fundamental modes of even (top) and odd symmetry.

Their interference results in a periodic transfer of power between the two ribs at a length of $L_c = \pi/(\beta_s - \beta_a)$, where β_s, β_a are the propagation constants of the symmetric and antisymmetric TE supermode. Table 2 compares the WMM results with values from Ref. [11].

		EIM	SIM	FEM	WMM
β/k	(s)	1.614021	1.611995	1.611412	1.610794
	(a)	1.612877	1.610369	1.609546	1.609100
$L_c/\ \mu$m		276	194	170	187

Table 2: Propagation constants β_s, β_a and coupling length L_c for the coupler of Figure 3, computed with the effective index approximation [11] (EIM), with the spectral index method [11] (SIM), a finite element program [11] (FEM), and the semivectorial wave matching method (WMM).

Due to the deep etching, the effective index results differ significantly, while there is a good agreement between the the more sophisticated methods. Note that neither the given SIM nor the FEM values can be guaranteed to be exact. The former suffer from the assumption of vanishing field at the inner sidewalls of the ribs (cf. Figure 4), the latter from a naturally limited mesh (cf. e.g. the benchmark test in Ref. [5]).

3.2 Arrow

The second example is not a coupler in narrower sense, but has a similar cross section. The dimensions of the antiresonant reflecting optical waveguide (ARROW) [12] as given in Figure 5 have been chosen [11] such that for each polarization one of its modes exhibits a large amplitude in the central region between the two small ribs. Figure 6 shows the corresponding profiles, computed with the semivectorial WMM.

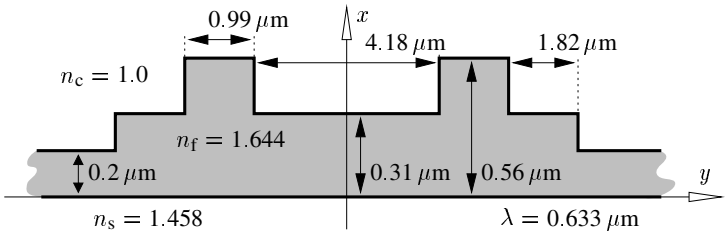

Figure 5: ARROW geometry and parameters, data from Ref. [11].

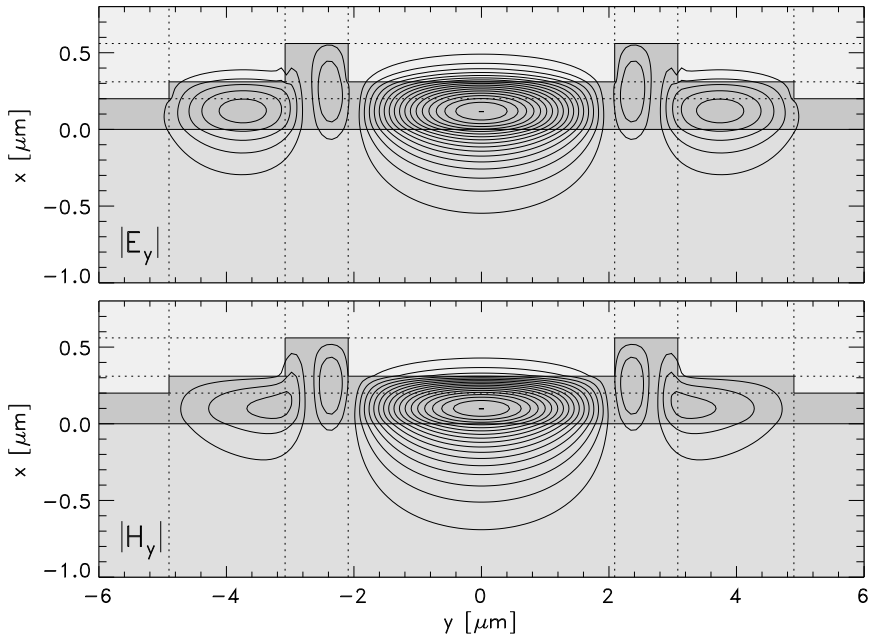

Figure 6: Field contours for the dominant components of the relevant TE (top) and TM (bottom) modes for the structure of Figure 5.

These modes have propagtion constants below the value of the planar waveguide corresponding to the stack of layers in the central region. They are not the fundamental modes, but those which will carry most of the power, if the structure is excited e.g. by the field of a fiber focused on the central region.

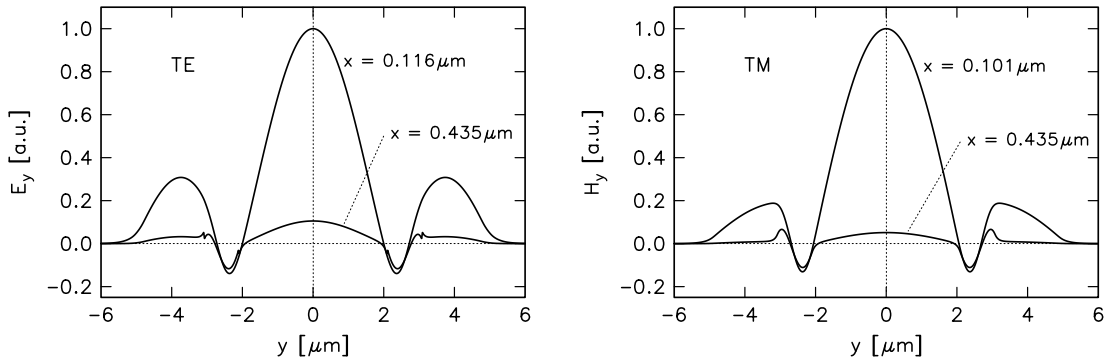

Figure 7: Profile cross sections of the dominant field components for the modes of Figure 6. E_y (TE mode, left) and H_y (TM mode, right) was evaluated on lines parallel to the y-axis, at the position of the maximum field amplitude ($x = 0.116\ \mu$m for TE, $x = 0.101\ \mu$m for TM) and at half the level of the protruding ribs, at $x = 0.435\ \mu$m.

The profile sections shown in Figure 7 can be directly compared with analogous plots in Ref. [11]. The good agreement especially with the fields from the spectral index method may be explained by the small amplitudes in the regions outside the ribs for $x > 0.31\,\mu$m, where the SIM assumes vanishing fields. The WMM gives access to the correct fields in these regions as well, as shown by the curves in Figure 7.

Table 3 compares propagation constants from the different methods. Agreement in the SIM and WMM fields is accompanied by a good agreement of the effective mode indices. At the same time, slightly smaller FEM mode

		EIM	SIM	FEM	WMM
β/k	TE	1.534432	1.534115	1.533470	1.534142
	TM	1.507001	1.506904	1.506720	1.506945

Table 3: Relevant TE and TM effective mode indices for the ARROW of Figure 5. Methods are named as in Table 2.

indices may be due to the limited FEM mesh size (73*109 Points [11]) and to the restriction on a computational window.

3.3 3-D coupler

Figure 8 gives the parameters for a three dimensional four waveguide coupler. Details on the proposal, simulation, and fabrication of such decvices have been reported in Ref. [13].

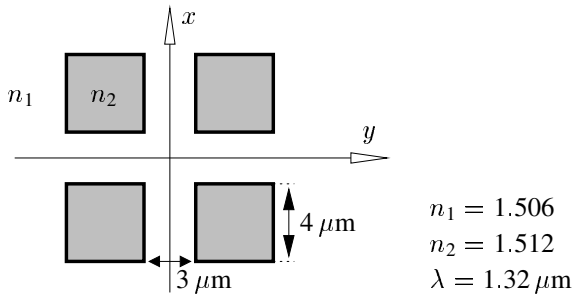

Figure 8: 3-D coupler parameters[13].

The cross section may be decomposed into 3×3 inner rectangular regions, therefore the device presents itself for a WMM simulation. At the same time the guiding refractive index is only about 4% higher than the cladding value, and this means somehow extreme conditions for the WMM. Nevertheless, the results are reasonable and agree well with the findings from Ref. [13]. Figure 9 shows profiles for the four TE polarized modes of the structure, Table 4 compares the corresponding mode indices.

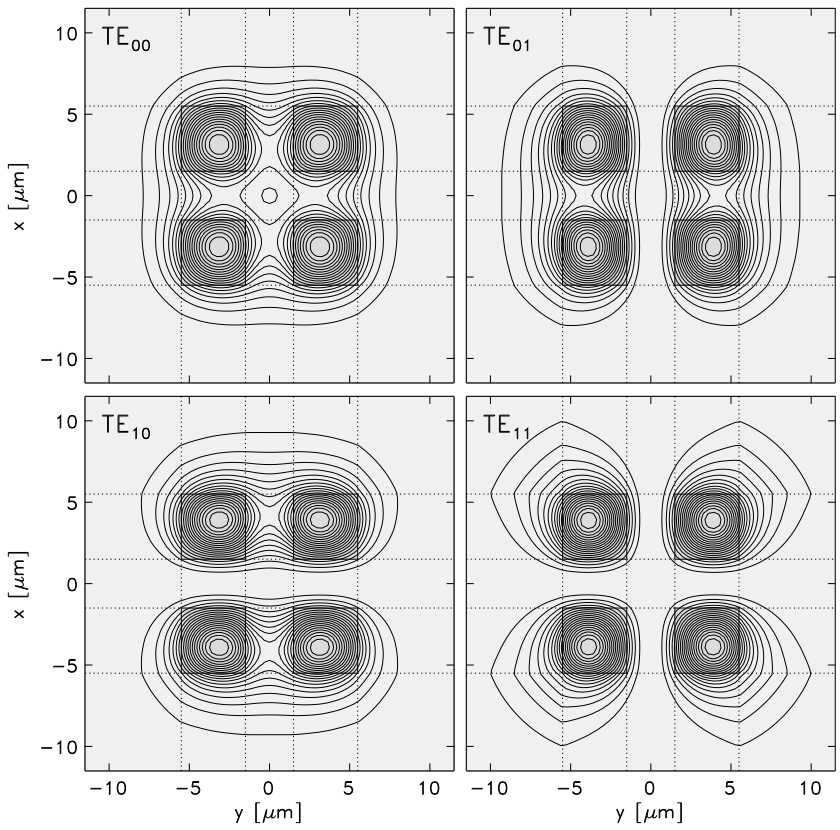

Figure 9: Intensity profiles for the four TE modes of the coupler sketched in Figure 8. The mode indices denote the number of horizontal and vertical nodal lines of the dominant E_y component.

	β_{00}/k	β_{01}/k	β_{10}/k	β_{11}/k	L_c
VFEM	1.5075807	1.5067966	1.5067966	1.5060266	850 μm
WMM	1.5078966	1.5071085	1.5071092	1.5064697	925 μm

Table 4: Effective mode indices β/k and coupling length L_c for the 3-D coupler of Figure 8. The line VFEM contains data from a vectorial finite element method [13], WMM are results from our semivectorial calculations.

The vectorial FEM mode indices are systematically slightly smaller than the values computed with the semivectorial WMM. Explanations may be the remaining error in the WMM field, apparent especially for the lowest order mode in Figure 9, or alternatively a retricted FEM computational window. There is also a small qualitative discrepancy: the FEM states exactly equal propagation constants of the two first order TE modes, the WMM predicts slightly different values for the modes with one horizontal respectively vertical nodal line in the dominant component. While due to the symmetry of the problem each TE mode is twofold degenerate with a corresponding TM mode, it is not a priori evident that the first order modes with the nodal line parallel and perpendicular to the direction of the polarization should be degenerate. The latter arguments supports the WMM result.

However, assuming degenerate TE_{01} and TE_{10} modes $\beta_{01} \approx \beta_{10}$ and equal differences $\Delta\beta \approx \beta_{00} - \beta_{10} \approx \beta_{10} - \beta_{11}$, one can define a coupling length $L_c = \pi/\Delta\beta$ for the power transfer between two diagonally opposite waveguides [13]. Values calculated with the corresponding averages are compared in the last column of Table 4.

3.4 Radiatively coupled waveguides

In this section we discuss a three waveguide arrangement as sketched in Figure 10 comprising two identical outer guides and a broad strip inbetween. The term radiative coupling [14] is motivated by viewing the structure as two leaky waveguides, where the power radiated by one waveguide is caught by the opposite one.

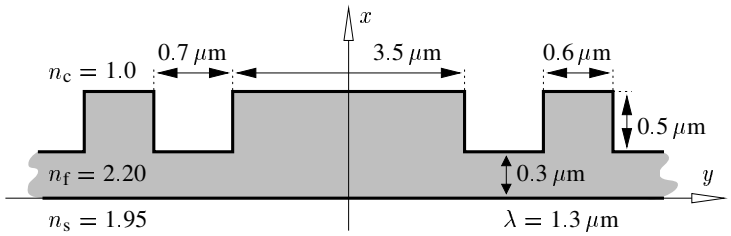

Figure 10: Radiatively coupled waveguide structure.

Alternatively, the entire structure may be regarded as a single lossless multimode waveguide. The simulation starts by computing the set of its guided modes. Semivectorial WMM mode analysis yields the six TE modes illustrated in Figures 11, 12.

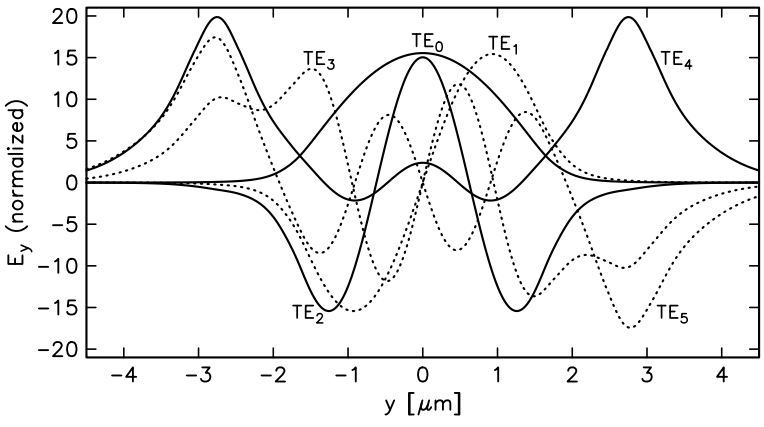

Figure 11: Profile cross sections for the six TE modes of the radiatively coupled waveguide structure. E_y has been evaluated on a line parallel to the y axis at $x = 0.15\,\mu$m. Continuous lines correspond to modes with even, dotted lines to modes with odd symmetry.

The coupler is to be excited by the single mode of one of the isolated outer waveguides. Figure 13 shows its profile. We assume a coupling section of a well defined length L, with the outer waveguides extended to form four input and output ports (cf. Figure 15). Let $\phi^a = (\boldsymbol{E}^a, \boldsymbol{H}^a)$ denote the six mode fields of the composed

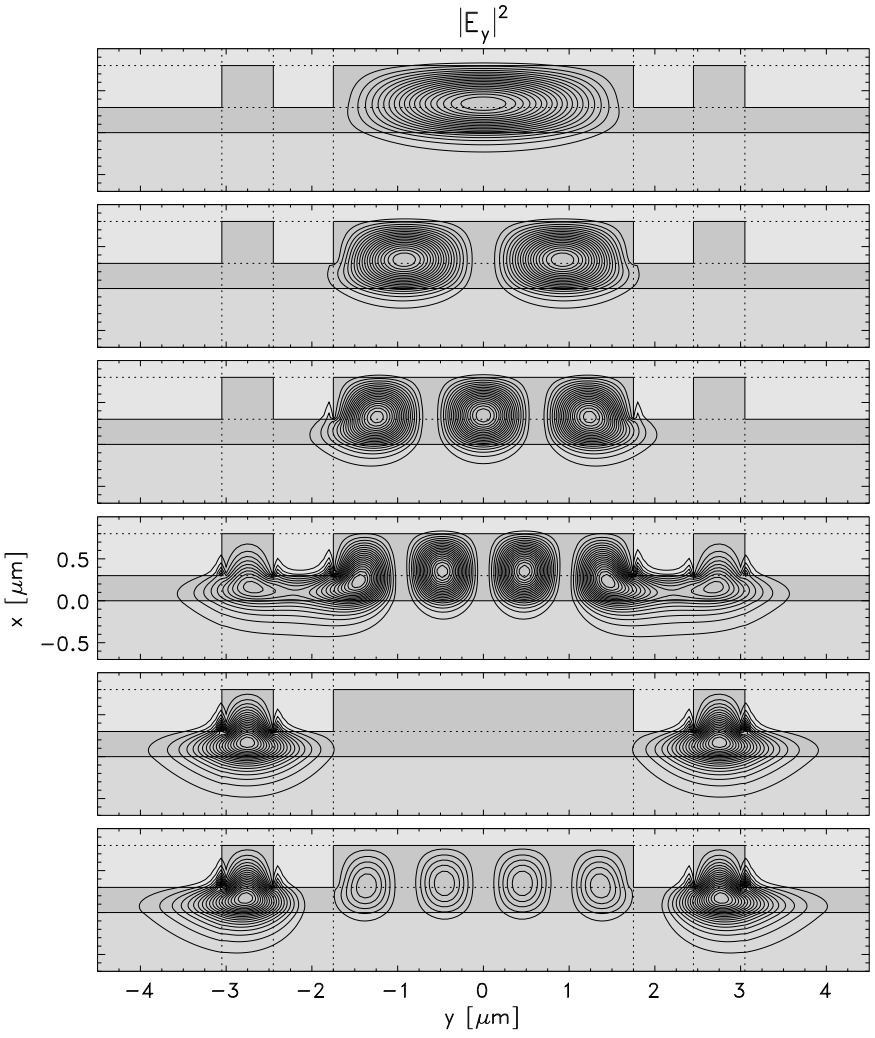

Figure 12: Intensity profiles for the TE modes of the coupler prescribed by Figure 10. The corresponding propagation constants $\beta/\,\mu\mathrm{m}^{-1}$ are

TE_0: 10.2232,
TE_1: 10.1171,
TE_2: 9.9417,
TE_3: 9.7185,
TE_4: 9.6789,
TE_5: 9.6595,

where the indices denote the number of vertical nodal lines in E_y.

structure, with propagation constants β^a. Analogously ϕ^{l} and ϕ^{r} are the modes of the left and right input respectively output ports, its propagation constant is β_*. Using the notation

$$(\boldsymbol{E}^a, \boldsymbol{H}^a | \boldsymbol{E}^b, \boldsymbol{H}^b) = \frac{1}{2} \iint (E_x^a H_y^b - E_y^a H_x^b)\, \mathrm{d}x\, \mathrm{d}y\,, \tag{13}$$

the involved modes are orthogonal according to $(\phi^a|\phi^b) = \delta_{ab}$, $(\phi^{\mathrm{r}}|\phi^{\mathrm{l}}) = 0$, where the latter equality holds due to the waveguide separation. All modes are assumed to be normalized with respect to Eq. (13).

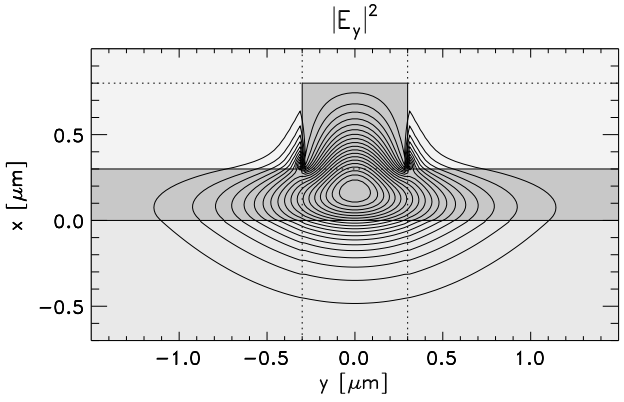

Figure 13: Fundamental TE mode of one isolated outer waveguide of the coupler in Figure 10. The corresponding propagation constant is $\beta_* = 9.6806\,\mu\mathrm{m}^{-1}$. Note the pronounced discontinuities in E_y at the sidewalls of the deeply etched rib.

Neglecting radiation and reflection at input and output, the power transferred to waveguide $j = \mathrm{l}, \mathrm{r}$ at $z = L$

after excitation at $z = 0$ in the left waveguide can be written

$$P_j(L) = \left| \sum_a (\phi^j | \phi^a)(\phi^a | \phi^1)\, \mathrm{e}^{\mathrm{i}\beta^a L} \right|^2 . \tag{14}$$

Chiefly those modes with a large overlap with the exciting field contribute to the power transfer. According to Figures 12, 13, these are the highest order modes, i.e. those with large field amplitudes in the regions of the outer waveguides and with propagation constants close to the level β_*. Together with additional small contributions form the remaining four modes, this results in the beating pattern plotted in Figure 14. Coupling between the outer waveguides is a truly multimode interference phenomenon.

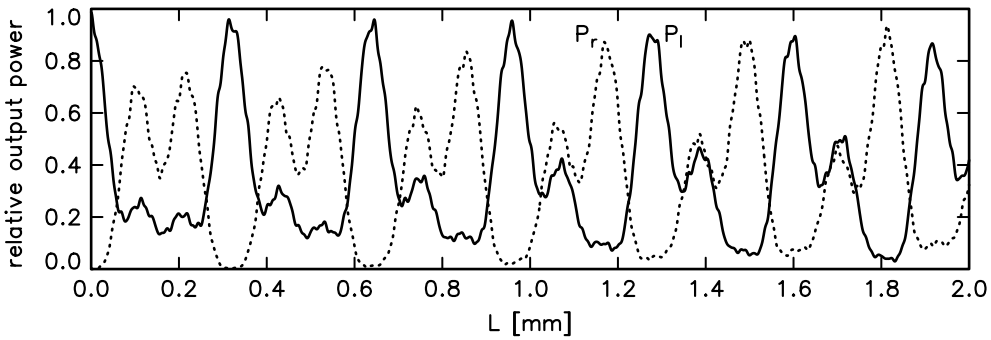

Figure 14: For the coupler of Figure 10: relative power transfer to the left outer waveguide P_l (continuous line) and to the right outer waveguide P_r (dotted line) versus the length L of the coupling section. The structure is assumed to be excited by the TE mode of the isolated left waveguide.

According to Figure 14, for a device length slightly below 1 mm, the power is concentrated in the input waveguide again. Figure 15 illustrates the light propagation for this length. For complete power transfer, the device needs a length of about two millimeters.

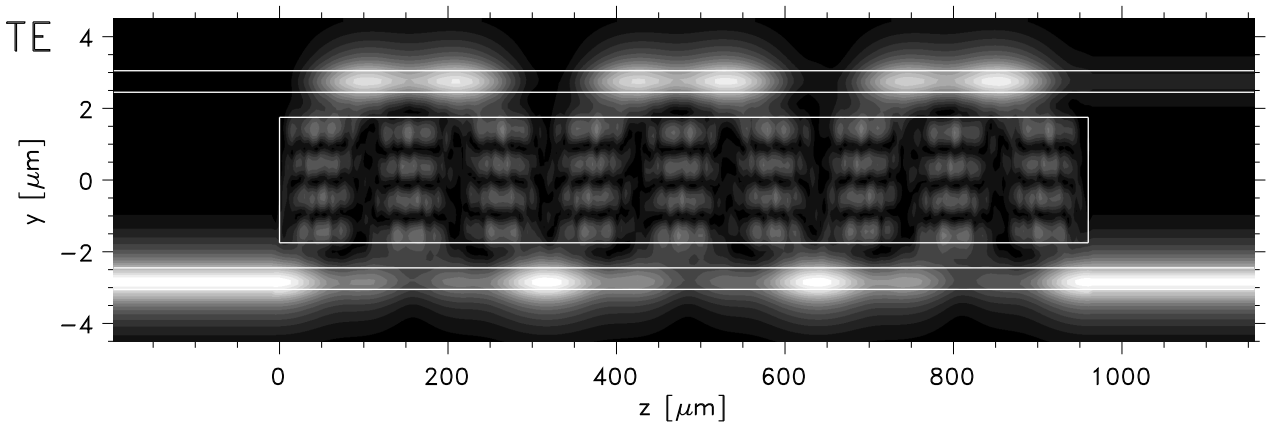

Figure 15: TE light propagation through a radiatively coupled waveguide structure with a cross section as given by Figure 10, with a coupling section of length $L = 960\,\mu$m. Greyscale levels correspond to the squareroot of the z-component of the Poynting vector, evaluated on the y-z-plane at $x = 0.15\,\mu$m.

With this structure a problem shows up, which is closely related to that discussed at the end of Section 2. Ideally all modes should be orthogonal with respect to the product (13). This orthogonality is not enforced by the mode solver, but should emerge if the mode fields are adequately approximated. Indeed, the overlap was zero (for modes with opposite symmetry) or very low (≈ 0.001) for most pairs, with the exception of the combination of the third and fifth order normalized modes (overlap ≈ 0.1). Note that these modes are of the same polarization and symmetry, and that both propagation constants are close to the propagation constant β_* of the outer waveguides, i.e. relatively closely spaced. Thus the unphysically large overlap may be understood

in the following way. If two modes are exactly degenerate, the WMM will arbitrarily select that superposition of both with the smallest error Eq. (5). If their propagation constants are farther apart, there may be a remainder of the other one in each calculated field, even if there are two separable parabolic sections in the error function. Numerically one cannot expect a discontinuous transition from 'degenerate' to 'nondegenerate'.

To overcome this problem, we followed the hint given at the end of Section 2. All results shown for this structure are computed with a normalization expression Eq. (8), where the part concerned with the rectangular regions of the outer waveguides has been multiplied by a factor of 5. This lowered the absolute overlap of the two supermodes in question to a value below 0.005, i.e. to the same order of magnitude as the overlaps of the other pairs. At the same time the properties of the remaining modes were almost unaffacted by this modification. This strategy was already applied to simulate radiatively coupled waveguide based isolator devices [15]. However, the somehow arbitrary modification must be regarded as an additional uncertainty for the simulation, and as a reason to switch to WMM-based coupled mode theory [16], when such situations are encountered.

4 Conclusion

For waveguides with piecewise constant and rectangular permittivity profiles, mode analysis can start with a simple ansatz of locally factorizing harmonic or exponential functions. A least squares expression for the mismatch in the continuity conditions on dielectric boundaries connects the fields on adjacent regions. Minimization of this error allows to identify propagation constants and to compute the mode fields.

While in principle the current implementation of this procedure allows to simulate cross sections with an arbitrary rectangular decomposition, the method turns out to be effective especially for structures described by few rectangles and boundary lines only. This class includes simple rib and raised strip waveguides as well as coupler geometries constructed from these waveguides. For the composite structures investigated in this paper, the WMM results are reasonable and accurate.

The method yields quasianalytical representations of the modal fields that are not restricted to a spatial computational window. It is thus well qualified as the basis in a larger computational design environment, for instance for propagating mode analysis as exemplified in Section 3.4, for coupled mode theory [16], or evaluation of perturbational expressions [17, 18].

Acknowledgment

Financial support by Deutsche Forschungsgemeinschaft (Sonderforschungsbereich 225) is gratefully acknowledged.

References

[1] D. Yevick. A guide to electric field propagation techniques for guided-wave optics. *Optical and Quantum Electronics*, 26:185–197, 1994.

[2] H. J. W. M. Hoekstra. On beam propagation methods for modelling in integrated optics. *Optical and Quantum Electronics*, 29:157–171, 1997.

[3] D. G. Hall and B. J. Thompson, editors. *Selected Papers on Coupled-Mode Theory in Guided-Wave Optics*, volume MS 84 of *SPIE Milestone Series*. SPIE Optical Engineering Press, Bellingham, Washington USA, 1993.

[4] K. S. Chiang. Review of numerical and approximate methods for the modal analysis of general optical dielectric waveguides. *Optical and Quantum Electronics*, 26:S113–S134, 1994.

[5] C. Vassallo. 1993-1995 Optical mode solvers. *Optical and Quantum Electronics*, 29:95–114, 1997.

[6] U. Rogge and R. Pregla. Vectorial Method of Lines for the Analysis of Strip-Loaded Optical Waveguides. *Journal of the Optical Society of America B*, 8:459–463, 1991.

[7] A. S. Sudbø. Film mode matching: a versatile numerical method for vector mode fields calculations in dielectric waveguides. *Pure and Applied Optics*, 2:211–233, 1993.

[8] M. Lohmeyer. Wave-matching method for mode analysis of dielectric waveguides. *Optical and Quantum Electronics*, 29:907–922, 1997.

[9] M. Lohmeyer. Vectorial wave-matching mode analysis of integrated optical waveguides. *Optical and Quantum Electronics*, 30:385–396, 1998.

[10] K. Mertens, B. Scholl, and H. J. Schmitt. New Highly Efficient Polarization Converters Based on Hybrid Supermodes. *Journal of Lightwave Technology*, 13(10):2087–2092, 1995.

[11] J. R. Pujol Pola, W. Biehlig, and F. Lederer. A Generalization of the Spectral Index Method Toward Multiple Rib Waveguides. *Journal of Lightwave Technology*, 14(3):454–460, 1996.

[12] M. A. Duguay, Y. Kokubun, and T. L. Koch. Antiresonant reflecting optical waveguides in SiO_2–Si multilayer structures. *Applied Physics Letters*, 49:13–15, 1986.

[13] L. Friedrich, P. Dannberg, C. Wächter, Th. Hennig, A. Bräuer, and W. Karthe. Directional coupler device using a three-dimensional waveguide structure. *Optics Communications*, 137:239–243, 1997.

[14] S. M. Loktev, V. A. Sychugov, and B. A. Usievich. Propagation of light in a system of two radiatively coupled waveguides. *Sov. Journal of Quantum Electronics*, 24(5):435–438, 1994.

[15] M. Lohmeyer, M. Shamonin, N. Bahlmann, P. Hertel, and H. Dötsch. Radiatively coupled waveguide concept for an integrated magneto-optic circulator. In K. Rubin, J. A. Bain, T. Nolan, D. Bogy, B. J. H. Stadler, M. Levy, J. P. Lorenzo, M. Mansuripur, Y. Okamura, and R. Wolfe, editors, *High-Density Magnetic Recording and Integrated Magneto-Optics: Materials and Devices*, volume 517 of MRS Symposium Proceedings Series, pages 519–524, 1998.

[16] M. Lohmeyer, N. Bahlmann, O. Zhuromskyy, and P. Hertel. Radiatively coupled waveguide polarization splitter simulated by wave-matching based coupled mode theory. *Optical and Quantum Electronics*, 1999. Accepted for publication.

[17] M. Lohmeyer, N. Bahlmann, and P. Hertel. Geometry tolerance estimation for rectangular dielectric waveguide devices by means of perturbation theory. *Optics Communications*, 163(1-3):86–94, 1999.

[18] M. Lohmeyer, N. Bahlmann, O. Zhuromskyy, H. Dötsch, and P. Hertel. Phase-matched rectangular magnetooptic waveguides for applications in integrated optics isolators: numerical assessment. *Optics Communications*, 158:189–200, 1998.